

Etoposide Induces Necrosis Through p53-Mediated Antiapoptosis in Human Kidney Proximal Tubule Cells

Hyuk-Kwon Kwon,^{*,1} Hyeon-Jun Shin,^{*,1} Jae-Hyeok Lee,^{*,1} Seol-Hee Park,^{*} Min-Cheol Kwon,^{*} Suresh Panneerselvam,^{*} Chan Gyu Lee,[†] Sang Geon Kim,[†] Jae-Ho Kim,^{*,2} and Sangdun Choi^{*,3}

^{*}Department of Molecular Science and Technology, Ajou University, Suwon 443-749, Korea and [†]College of Pharmacy and Research Institute of Pharmaceutical Sciences, Seoul National University, Seoul 151-742, Korea

¹These authors contributed equally to this study.

²To whom Co-Correspondence should be addressed at J.H. Kim, Department of Molecular Science and Technology, Ajou University, Suwon 443-749, Korea. E-mail: jhkim@ajou.ac.kr

³To whom correspondence should be addressed at Department of Molecular Science and Technology, Ajou University, Suwon 443-749, Korea. Fax: +82-31-219-1615. E-mail: sangdunchoi@ajou.ac.kr

ABSTRACT

The p53 protein is an important transcription factor that modulates signaling pathways for both cell death and survival. Its antiapoptotic mechanisms that correlate with necrotic and apoptotic cell death are not well understood. Here, we report that etoposide promotes progression of the DNA damage response as well as necrotic morphological changes including plasma membrane rupture using carbon nanotube-tipped/atomic force microscopy (CNT/AFM) probes in human kidney proximal tubule (HK-2) cells. Inhibition of p53 abrogated cell cycle arrest and led to a decrease in the expression levels of repair proteins that were induced by DNA damage. Mitochondrial biogenesis and cytosolic production of reactive oxygen species were also reduced after p53 inhibition; the latter change induced mitochondrial superoxide accumulation and mitochondrial damage, which triggered the activation of caspase 3. Inhibition of p53 also led to a loss of cell adhesion and converted necrotic cell death to apoptotic cell death, with appreciable cell shrinkage and appearance of apoptotic bodies that were observed using CNT/AFM probes. Thus, our study demonstrated that p53 protects against apoptosis, and leads to etoposide-induced necrosis. These results are expected to aid in the understanding of mechanism of antiapoptosis and its relationship to cell death.

Key words: antiapoptosis; apoptosis; etoposide; necrosis; p53

The tumor suppressor protein, p53, is involved in the transcriptional induction of various vital cellular proteins induced in response to oxidative stress. These cellular proteins are involved in DNA damage repair, cell cycle arrest, and mitochondrial respiration, ultimately resulting in antiapoptosis and protection from DNA damage (Janicke *et al.*, 2008; Vousden and Lane, 2007). More than 75% of cancers involve loss-of-function and other mutations in p53, thus suggesting a crucial role for this protein in cancer development (Muller and Vousden, 2013). There is also evidence that p53 contributes to mitochondrial biogenesis: in p53 knockout mice, there is a decrease in the mitochondrial

yield and the expression level of peroxisome proliferator-activated receptor-gamma coactivator-1 α (PGC-1 α) (Saleem *et al.*, 2009). Mitochondrial biogenesis is regulated by nuclear-encoded transcription factors [transcription factor A, mitochondrial (TFAM)] and coactivator proteins (PGC-1 α and PGC-1 β), which are activated by DNA damage-inducing chemicals, thereby contributing to metabolism and antioxidant defense processes (Fu *et al.*, 2008; Hock and Kralli, 2009; Weinberg, 2011). Mitochondria are involved in cellular metabolism, differentiation, and signaling. They play an important role in the regulation of the cell cycle, including processes associated with cell

death. Adenosine triphosphate (ATP) is produced via mitochondrial respiratory chain complexes I through V in the inner membrane (Zhang and Guterman, 2007), and dysfunction of this pathway is closely related to many diseases affecting the brain, muscles, nerves, kidneys, and others (McBride et al., 2006; Pieczenik and Neustadt, 2007). Mitochondrial respiratory complexes I and III are known to generate superoxide (O_2^-) in the matrix and intermembrane space, and known to release reactive oxygen species (ROS) into the cytosol via ion channels (West et al., 2011). Generation of ROS such as O_2^- , H_2O_2 , and the hydroxyl radical causes damage to nucleic acids and proteins, and initiates a variety of cellular processes (Ray et al., 2012). A recent study demonstrated that p53 interacted directly with cyclophilin D in the mitochondrial matrix and triggered the opening of mitochondrial permeability transition pores, ultimately resulting in necrosis, oxidative stress, and ischemia (Vaseva et al., 2012). However, the initiation of cell antiapoptotic mechanisms mediated by p53 and their relation to mitochondrial alteration and/or ROS migration processes during necrotic and apoptotic cell death are not fully understood at present.

Our study demonstrated that etoposide (ETO)-induced DNA damage led to necrosis and triggered apoptosis due to prolonged DNA damage, and that p53 drove antiapoptotic processes and maintained ETO-induced necrosis in HK-2 cells. However, apoptosis was triggered directly in p53-deficient cells.

MATERIALS AND METHODS

Cell culture and treatments. The normal human kidney cell line (HK-2, American Type Culture Collection, Manassas) was grown in the RPMI 1640 medium (Thermo Fisher Scientific, Inc, Massachusetts) containing 1% penicillin/streptomycin and 10% FBS (fetal bovine serum; Thermo Fisher Scientific, Inc); the medium was changed after overnight incubation in a humidified atmosphere containing 5% CO_2 at 37°C. The mouse embryonic fibroblast (MEF) cell line was grown as previously described (Kim et al., 2010). ETO or DOX or H_2O_2 (Sigma-Aldrich, St. Louis, Missouri) was added to the culture medium and p53 inhibitor (PFT- α ; Sigma-Aldrich) or ERK inhibitor (PD98059; Sigma-Aldrich) pretreatment (where appropriate) was performed 1 h before treatment with ETO.

Cell viability analysis. A colorimetric 1-(4,5-dimethylthiazol-2-yl)-3,5-diphenylformazan (MTT) solution (Sigma-Aldrich) was used for determining cell viability. The cells were grown overnight (seeded at 5×10^3 /well) in 96-well plates (BD Biosciences, San Jose, California); subsequently, the cells were treated as follows: the MTT mixture solution (100 μ l/well) was added and incubated for 3 h at 37°C. We then removed the MTT-containing supernatant, added DMSO (dimethyl sulfoxide) solution (100 μ l/well), and incubated the plates for 30 min at room temperature. The plates were read on a microplate spectrophotometer system (Molecular Devices, Silicon Valley, California) at 540 nm.

Cytotoxicity analysis. The cells were grown overnight (seeded at 5×10^3 /well) in 96-well plates (BD Biosciences) and treated with indicated condition. Cytotoxicity was measured using LDH Cytotoxicity Detection Kit (Takara Bio, Inc, Otsu, Shiga, Japan) according to the manufacturer's protocol. The plates were read using microplate spectrophotometer (Molecular Devices) at 490 nm.

Cytosolic ATP analysis. Cells (4×10^5 per 6 cm dish) were counted using a hematology analyzer and seeded (10^4 /well) in 96-well plates (Greiner Bio-One, Baden-Württemberg, Germany). Cytosolic

ATP was quantified using the CellTiter-Glo Luminescent Cell Viability Assay kit (Promega, Madison, Wisconsin) according to the manufacturer's protocol using a SPECTRAMax GEMINI fluorescence microplate reader (Molecular Devices).

Caspase 3/7 activity analysis. Cells (4×10^5 per 6 cm dish) were counted using a hematology analyzer and seeded (10^4 /well) in 96-well plates (Greiner Bio-One). Activity of caspases 3 and 7 was measured using the Caspase-Glo 3/7 Assay (Promega) according to the manufacturer's protocol using SPECTRAMax GEMINI fluorescence microplate reader (Molecular Devices); the luminescence intensity was measured using a Fuji LAS-3000 system (Fuji Film Life Science, Tokyo, Japan).

NO secretion analysis. Cells (4×10^5 per 6 cm dish) were plated and the supernatant (1 ml) was collected from each sample. Syringe filters (pore size 0.22 μ m; BD Biosciences) were used for filtering supernatant media. Supernatant samples (100 μ l) and nitric oxide standards (range: 100 μ M to 0.1 μ M) were seeded in 96-well plates. N2 buffer (50 μ l; iNtRON Biotechnology Inc., Sungnam, Korea) was added to the wells for 10 min and then 50 μ l of N1 buffer was added at room temperature for overnight incubation. NO secretion was analyzed on a microplate spectrophotometer system (Molecular Devices) at 550 nm.

Western blot analysis. Whole protein extraction solution (M-PER; Thermo Fisher Scientific, Inc.) and a protease and phosphatase inhibitor cocktail (Thermo Fisher Scientific, Inc.) were added to the cell pellets for 10 min at 4°C, and the lysates were centrifuged at $16\,000 \times g$ for 10 min. The protein concentration was measured using the BCA method (Sigma-Aldrich). Equal amounts of protein samples (40–50 μ g) were separated in a 10–12% SDS-polyacrylamide gel and transferred to nitrocellulose membranes (Hybond ECL; Amersham Pharmacia Biotech Inc, Piscataway, New Jersey) using a transfer buffer maintained at 4°C. The membranes were blocked with 5% nonfat dried milk for 1 h and were then immunoblotted overnight with specific primary antibodies (1:500–1000) to the following proteins: PARP1, γ -H2AX (ser139), MDM2, p53, p-p53 (ser15), p-p53 (ser392), p-ATM (ser1981), p-ERK (thr202 and tyr204), Bcl2, 53BP1, BRCA1, β -actin, caspase 3, COX-2, iNOS (Santa Cruz Biotechnology Inc, Dallas), or p-CHK2 (thr68), H2AX, p53, ATM, CHK2, and ERK (Cell Signaling Technology Inc., Danvers, Massachusetts). After the membranes were washed 5 times with PBS-T (0.05% Tween 20 in phosphate-buffered saline), they were incubated with a peroxidase-conjugated anti-mouse or anti-rabbit IgG antibody (1:1000) for 2 h. Proteins were detected using either the SuperSignal West Pico ECL solution (Thermo Fisher Scientific, Inc.) and X-ray film or the Fuji LAS-3000 system (Fuji Film Life Science). The intensity of the cleaved-caspase 3 band was calculated using the ImageJ software (Schneider et al., 2012).

Cell cycle analysis (PI staining). Cells (4×10^5 per 6 cm dish) were collected, washed with 3 ml of phosphate-buffered saline (PBS), and centrifuged at $200 \times g$ for 5 min. The cell suspension was added into a tube containing 70% cold ethanol and 30% cold PBS. After that, the cells were kept overnight at 4°C for fixation, were centrifuged at $200 \times g$ for 5 min, and then washed with 1 ml of PBS. Single-cell suspensions were labeled with PI (50 μ g/ml) and RNase A was added (500 μ g/ml; Sigma-Aldrich). After that cells were analyzed using FACSaria III with the Diva software (BD Biosciences).

Apoptosis and necrosis analysis (annexin V/PI double staining). Cells (4×10^5 per 6 cm dish) were collected, washed with 3 ml of PBS,

and centrifuged at $200 \times g$ for 5 min. Binding buffer (100 μ l) was added to the cells, and they were labeled with the Annexin V dye (10 μ l) and the PI dye (10 μ l) (BD Biosciences) for 15 min at room temperature. The binding buffer (200 μ l) was added and the mixture was kept at 4°C. Cells were analyzed using FACSaria III with the Diva software (BD Biosciences).

Mitochondrial superoxide analysis (MitoSox staining). For this purpose, 5 μ M MitoSox (Life Technologies, Grand Island) solution was added for 15 min to the cells in the presence of 5% CO₂ at 37°C. The cells were harvested by trypsinization (2 min), washed with 3 ml PBS, and centrifuged at $200 \times g$ for 5 min. After the supernatant was removed, PBS (300 μ l) was added to the pellets and they were kept on ice (4°C). Cells were analyzed using FACSaria III with the Diva software (BD Biosciences).

Mitochondrial biogenesis analysis (MitoTracker Red CMXRos/Green FM double staining). After incubation of the cells with MitoTracker CMXRos and/or Green FM (Life Technologies) solutions (100 nM) for 15 min, in the atmosphere containing 5% CO₂ at 37°C, the cells were harvested by trypsinization (2 min), washed with 3 ml PBS, and centrifuged at $200 \times g$ for 5 min. After the supernatant was removed, PBS (300 μ l) was added to the pellets and they were kept on ice (4°C). Cells were analyzed using FACSaria III with the Diva software (BD Biosciences).

Analysis of cytosolic NO and ROS (DAF-FM and DCF-DA staining). Three milliliters of PBS was added to the cells, which were then treated with DAF-FM (1 μ l [5 μ M]) and DCF-DA (1 μ l [10 μ M]) at 37°C for 1 h and for 15 min, respectively. The cells were centrifuged at $200 \times g$ for 5 min, and PBS (300 μ l) was added to the pellets, which were then kept on ice (4°C).

Cell size analysis. Live cells were analyzed by means of FACSaria III with the Diva software (BD Biosciences) using forward scatter units (FSC; cell size) and side-scattered light (SSC, cell granularity). FSC intensity was analyzed using WinMDI software version 2.8 (Joseph Trotter, <http://facs.scripps.edu/software.html>).

Confocal microscopy. Cells (10^4 /well) were fixed with 3.7% formaldehyde in PBS for 15 min and permeabilized with 0.2% Triton X-100 for 15 min. The cells were incubated for 1 h with primary antibodies (1:1000) against γ -H2AX, PARP1, p-ATM, p-p53^{ser15}, p-p53^{ser392}, MDM2, 53BP1, BRCA1 (Santa Cruz Biotechnology Inc.), or p-CHK2 (Cell Signaling Technology Inc.) after blocking with 5% FBS for 1 h. Next, the cells were incubated for 1 h with a secondary antibody conjugated with either Alexa Fluor 488 or Alexa Fluor 546 (Life Technologies). For staining of nuclei, the cells were incubated with Hoechst 33258 (5 μ M; Sigma) for 15 min. We used confocal microscopy for imaging (LSM-700, Carl Zeiss Microscopy GmbH, Munich, Germany), and the data were analyzed using the Zen 2009 software package (Bolte and Cordelières, 2006).

Phase contrast microscopy. Cells (4×10^5 per 6 cm dish) were examined for morphological changes under a phase contrast microscope (E-scope i304, Macrotech, Goyang, South Korea) and the micrographs were analyzed using the Scopephoto software package.

MtDNA Copy number and mRNA levels. Cells were plated at 4×10^5 per 6 cm dish. Total DNA and RNA were extracted using the QuickGene SP kit (Fuji Film Life Science) according to the manufacturer's instructions and were quantified on a Micro UV-Vis

fluorescence spectrophotometer (MALCOM CO., LTD., Tokyo, Japan). The mtDNA copy number and mRNA levels were measured using a QuantiTect SYBR Green PCR Kit (Qiagen) and real-time PCR (Rotor-Gene Q, Qiagen, Valencia) with primers for ND4 (mtDNA), TFAM, PGC-1 α , and PGC-1 β (mRNA) as described previously (Bogacka *et al.*, 2005), and for GAPDH (5'-CCA CCC ATG GCA AAT TCC ATG GCA-3' and 5'-TCT AGA CGG CAG GTC AGG TCC ACC-3'). The PCR protocol was as follows: 10 min at 95°C; 30 cycles each of 5 s at 95°C and 10 s at 57°C for mtDNA (2 steps); and 30 cycles each of 5 s at 95°C, 10 s at 57°C, and 60 s at 72°C for mRNA (3 steps). Relative mtDNA and mRNA levels were calculated using the $\Delta\Delta$ CT method; both the mtDNA and mRNA levels of a target gene were normalized to GAPDH using the Rotor-Gene Q Series Software, version 2.2.3.

Analysis of the oxygen consumption rate. This rate was assessed by continuously moving a Clark-type electrode in a sealed chamber maintained at 37°C (Oxytherm System, Hansatech Instruments Ltd, UK). For cell-based assays, the cells were suspended in the culture medium at the concentration of 6×10^6 /ml. O₂ consumption of the total cells loaded into the chamber was measured, and an empty medium (without cells) was used as a control.

Analysis of cell swelling and cell adhesion efficiency. Harvested cells were counted using a hemocytometer (Marienfeld-Superiors, Lauda-Königshofen, Germany), seeded (10^5 /well in media [100 μ l]) on E-Plate 16 devices, and were then analyzed using the xCELLigence system (RTCA DP Analyzer, Roche Applied Science, Sandhofer, Germany) in a humidified atmosphere containing 5% CO₂ at 37°C. Real-time monitoring of electrical impedance (cell index, proportional to cell adhesion) was performed at 10-s intervals for 3 h, and the data were analyzed using the RTCA DP software (version 1.2).

Analysis of cell morphology and topography of the plasma membrane. Cells (10^4 per 6 cm dish) were fixed with 3.7% formaldehyde in PBS for 15 min and washed 3 times with PBS and deionized water. All AFM images were acquired in the noncontact mode on an XE-100 AFM system (Park systems, Inc., Suwon, South Korea) with CNT/AFM probes under usual ambient conditions. The CNT/AFM probes vibrated with a resonance frequency of approximately 310 kHz. Image analysis was performed using the XEI software (Park systems, Inc.). The morphology, length, width, height, and volume of the cells were directly determined from the images. The grain view analysis program is useful for gathering information on the cell volume in the AFM images loaded in the XEI software. Using the grain view program, surface profile parameters such as length, width, height, and volume of each detected grain can be calculated. After automatic grain detection, XEI can calculate surface profile parameters of the detected grains of the cell. We calculated the cell volume in the grain view program of the XEI software using the threshold method.

A knockdown of p53 using siRNA. Cells (2×10^5 per 6 cm dish) were transfected with p53 siRNA using the FuGENE HD Transfection Reagent (Promega) according to the manufacturer's instructions. Scrambled (negative control) and p53 siRNA were obtained from Genolution Pharmaceuticals (Seoul, Korea), and the sequence of the p53 siRNA was as follows: 5'-GAC UCC AGU GGU AAU CUA C-3' (Mahyar-Roemer and Roemer, 2001). After 24 h, media were changed, and cell samples were used for the subsequent experiments.

Statistical analysis. All calculations were performed using 1-way ANOVA within the SigmaPlot software, version 12.0 (Systat Software Inc, San Jose). All experiments were independently repeated at least 3 times, and statistical significance was defined as a P-value either * < 0.05 or ** < 0.01.

RESULTS

ETO-Induced DNA Damage Response (DDR) Proteins, Formation of γ -H2AX Foci, and Cell Cycle Arrest

ETO is a widely used chemotherapeutic drug that causes DNA damage by stabilizing covalent complexes of topoisomerase II with DNA, thereby leading to genotoxicity and cytotoxicity (Nitiss, 2009; Ross et al., 1984). DNA-damaging chemotherapeutic drugs have been reported to induce double- and single-strand breaks, which increase the expression levels of proteins participating in the DDR, namely, phosphorylated H2A histone family member X (γ -H2AX) and cleaved-poly (ADP-ribose) polymerase 1 (C-PARP1) (Rogakou et al., 2000; Soldani et al., 2001). Necrosis- and apoptosis-inducing chemicals induce the expression of C-PARP1 (55 and 89 kDa) via the expression of lysosomal protease and caspase 3, respectively (Gobeil et al., 2001). Figure 1 demonstrates both the cytotoxic effects of ETO and the expression levels of γ -H2AX and C-PARP1 in a dose- and time-dependent manner in HK-2 cells. Compared to untreated cells, ETO (50 μ M)-treated cells showed a 31.9% reduction in cell viability after 48 h of treatment (Fig. 1A). The expression level of γ -H2AX increased in a dose- and time-dependent manner. The expression levels of PARP1 (116 kDa) and the proapoptotic C-PARP1 (89 kDa) protein increased after only 48 h, whereas the expression level of the pronecrotic C-PARP1 (55 kDa) started increasing immediately in a time-dependent manner (Fig. 1A–C). Similarly, we observed increases in the fluorescence intensity of γ -H2AX and PARP1 but they did not co-localize to the nucleus (Fig. 1F).

A recent study reported that the DDR requires the expression of DNA damage sensors, transducers, mediators, and effectors, including ataxia telangiectasia mutated (ATM), ataxia telangiectasia and Rad3-related (ATR), checkpoint kinase1 (CHK1), checkpoint kinase2 (CHK2), p53, breast cancer 1, early onset (BRCA1), and p53-binding protein 1 (53BP1), in order to activate the relevant signaling pathways for cell death and survival (Nitiss, 2009; Polo and Jackson, 2011). In our study, we observed an increase in the phosphorylation of p53 on serine 15 (p-p53^{ser15}) and serine 392 (p-p53^{ser392}), and in the phosphorylation of ATM (p-ATM), as well as an increase in the expression levels of BRCA1 and 53BP1. There was also a decrease in the expression level of mouse double-minute 2 homolog protein (MDM2) (Fig. 1D). The fluorescence intensity of γ -H2AX/p-ATM, p-ATM/p-CHK2, γ -H2AX/53BP1, and 53BP1/BRCA1 increased. The signals were co-localized in the nucleus, suggesting that these proteins interacted with one another (Fig. 1G–L and Supplementary Fig. 1A). p-p53^{ser15} and p-ATM were co-localized and their overlap coefficients were increased by ETO in the nucleus (Supplementary Fig. 1B–E). MDM2 and p-p53^{ser15} decreased and increased in fluorescence intensity, respectively, but were not co-localized in the nucleus (Supplementary Fig. 2A). In particular, p-p53^{ser15} was expressed in both the cytosol and the nucleus, whereas p-p53^{ser392} was detected only in the cytosol (Fig. 1J and Supplementary Fig. 2B). Previous study described cell cycle arrest as an attempt to repair DNA damaged by ultraviolet light (UV), ionizing radiation (IR), and chemotherapeutic drugs (Dasika et al., 1999). Our results showed an increase in sub-G1 phase cells (DNA damage) and a decrease in the

proportion of the G1 phase cells during ETO treatment. ETO induced G2/M-phase arrest after S-phase arrest (Fig. 1E).

ETO-Induced Oxidative Stress and Mitochondrial Biogenesis

Oxidative stress such as nitric oxide (NO) and ROS generated by the mitochondrial respiratory chain can cause cell death by necrosis or apoptosis (Poyton et al., 2009; Ryter et al., 2007). Topoisomerase II-targeting drugs such as doxorubicin (DOX) have been reported to stimulate mitochondrial proliferation, as well as NO and ROS generation during cell death (Kluza et al., 2004; Mukhopadhyay et al., 2009). According to our results, ETO increased cytosolic NO (Fig. 2A) and NO secretion (Supplementary Fig. 3A). ETO also increased the expression levels of cyclooxygenase 2 and iNOS after 48 h of treatment (Supplementary Fig. 3B). We further found that ETO enhanced cytosolic ROS (cROS) generation (Fig. 2B).

Next, we assessed mitochondrial mass and respiration after ETO treatment using double staining with MitoTracker Red CMXRos (MTR) and MitoTracker Green FM (MTG). MTR enters mitochondria depending on the membrane potential, and thus, detects only respiring mitochondria. MTG detects all mitochondria (ie, mitochondrial mass), independently of the mitochondrial membrane potential. Figure 2 shows a shift in efficiency from the P3 to the P4 region compared to untreated cells (Fig. 2C). MTR and MTG intensity was also increased 1.8- and 2.0-fold, respectively (Fig. 2D). To further examine the effects of ETO on mitochondrial biogenesis, we analyzed the mRNA expression levels of transcription factor (TFAM) and coactivators (PGC-1 α and PGC-1 β). TFAM is a nuclear-encoded transcription factor and is controlled by PGC-1 α , which has been shown to enhance transcription and replication of mitochondrial DNA (mtDNA) (Ventura-Clapier et al., 2008). PGC-1 β performs a key function in mitochondrial biogenesis by increasing both the concentration of oxygen and its consumption rate (Meirhaeghe et al., 2003). We observed elevated expression levels of TFAM, PGC-1 α , and PGC-1 β compared to controls (Fig. 2E–G). The mtDNA copy number of NADH dehydrogenase subunit 4 (ND4) increased after ETO treatment (Fig. 2H). Upon confirmation of this change, we found an increase in cytosolic ATP production levels and an increase in the O₂ consumption rate (Fig. 2I and J).

Inhibition of p53 Abrogated Cell Cycle Arrest and Induction of DDR Proteins: Events That Enhanced ETO-induced DNA Damage and Cytotoxicity

The upregulation of p53 and DDR proteins in response to ETO resulted in cell cycle arrest and DNA damage repair in our ETO-treated cells, as expected (Alexieva-Botcheva and Anderson, 2012; Haupt et al., 2003). We further analyzed the p53 response to ETO using a pharmacological inhibitor of p53, pifithrin- α (PFT- α). Inhibition of p53 significantly increased the cytotoxicity in HK-2 cells by reduction of cell viability and induction of LDH release (Fig. 3A and B). Similarly, the inhibition of p53 resulted in the induction of ETO-induced cytotoxicity in mouse embryonic fibroblast (MEF) cells after 48 h when compared with ETO-treated cells (Supplementary Fig. 4B). On the other hand, the inhibition of p53 did not have significant regulatory effect on DOX-induced cytotoxicity in HK-2 and MEF cells when compared with DOX-treated cells (Supplementary Fig. 4A and B). The number of cells in the sub-G1 phase (DNA damage) increased, but a time-dependent decrease in the proportion of cells in the S phase and G2/M phase was observed in the cells that were cotreated with ETO and PFT- α (Fig. 3C).

To test whether inhibition of p53 affects the expression of proteins involved in DDR signaling pathways, we outperformed a

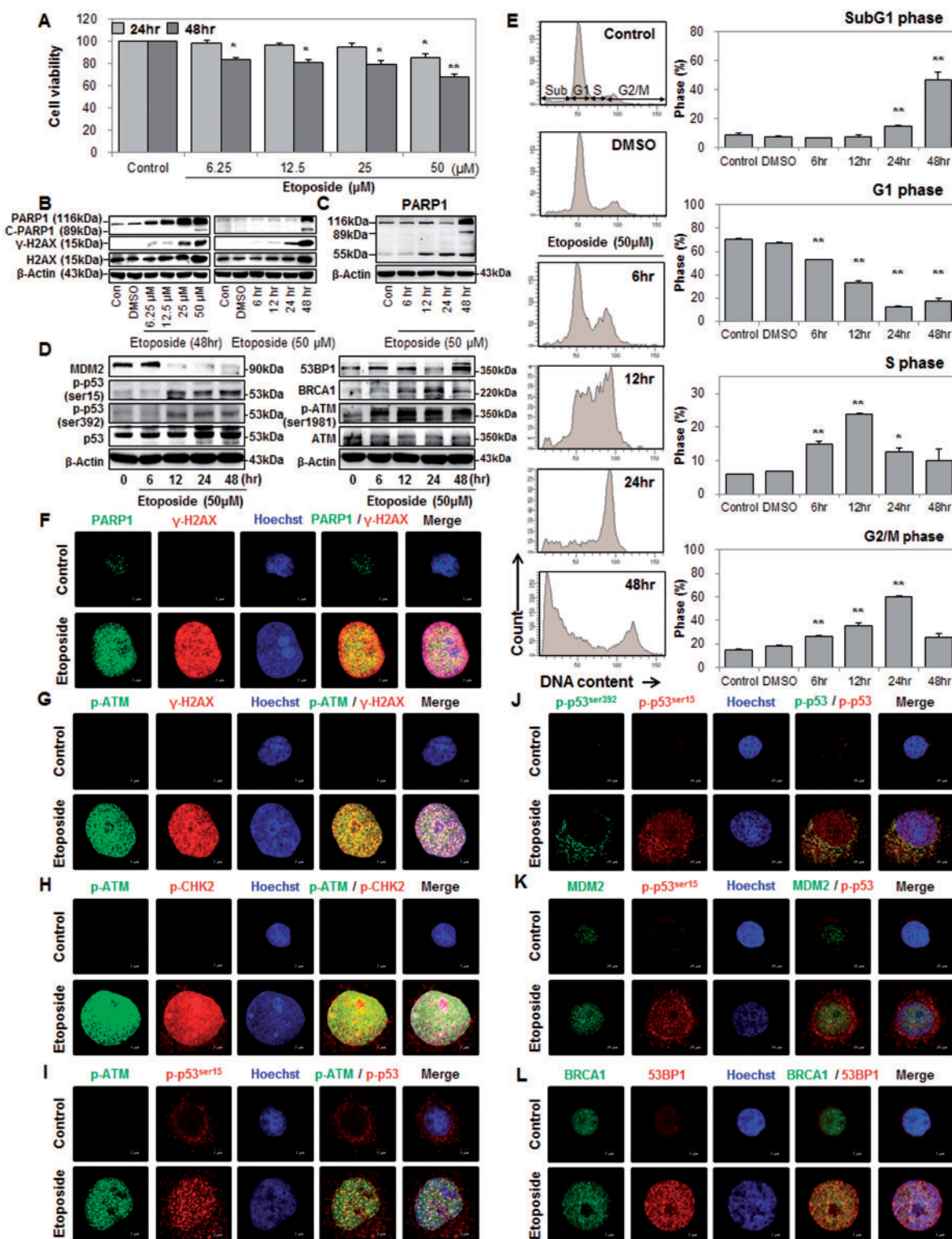


FIG. 1. Etoposide (ETO) induced DNA damage repair (DDR) proteins, formation of γ -H2AX foci, and an S and G2/M phase cell cycle arrest. We used HK-2 cells for the experiments and whole-cell extracts for Western blot analysis; β -Actin was used as a loading control. A, Cell viability was measured using the MTT assay using cells incubated with DMSO (control) and various doses of ETO for 24 and 48 h. B, Expression levels of PARP1, C-PARP1 (89 kDa), γ -H2AX^{ser139}, and H2AX with increasing doses and periods of ETO treatment were analyzed using Western blotting. C, PARP1 and C-PARP1 (89 and 55 kDa) expression levels were determined in ETO-treated cells at different time points using Western blotting. D, Expression levels of MDM2, p-p53^{ser15}, p-p53^{ser392}, p53, 53BP1, BRCA1, p-ATM^{ser1981}, and ATM proteins were analyzed using Western blotting at different time points of ETO treatment. E, The cells were either not treated (control) or treated with DMSO or ETO for the indicated periods. The cells were analyzed using PI staining and FACS analysis, and cell cycle phases are presented (* $P < 0.05$, ** $P < 0.01$). F–L, Confocal microscopy was used to examine the expression levels of PARP1, p-ATM^{ser1981}, γ -H2AX^{ser139}, p-CHK2^{thr68}, p-p53^{ser15}, p-p53^{ser392}, MDM2, 53BP1, and BRCA1 after the cells were incubated with ETO for 48 h. Representative microscopy images are shown: green staining (PARP1, p-ATM^{ser1981}, p-p53^{ser392}, MDM2, and BRCA1), red staining (γ -H2AX^{ser139}, p-p53^{ser15}, p-CHK2^{thr68}, and 53BP1), and blue staining (Hoechst 33258 for DNA [nucleus]). See also Supplementary Figures 1 and 2.

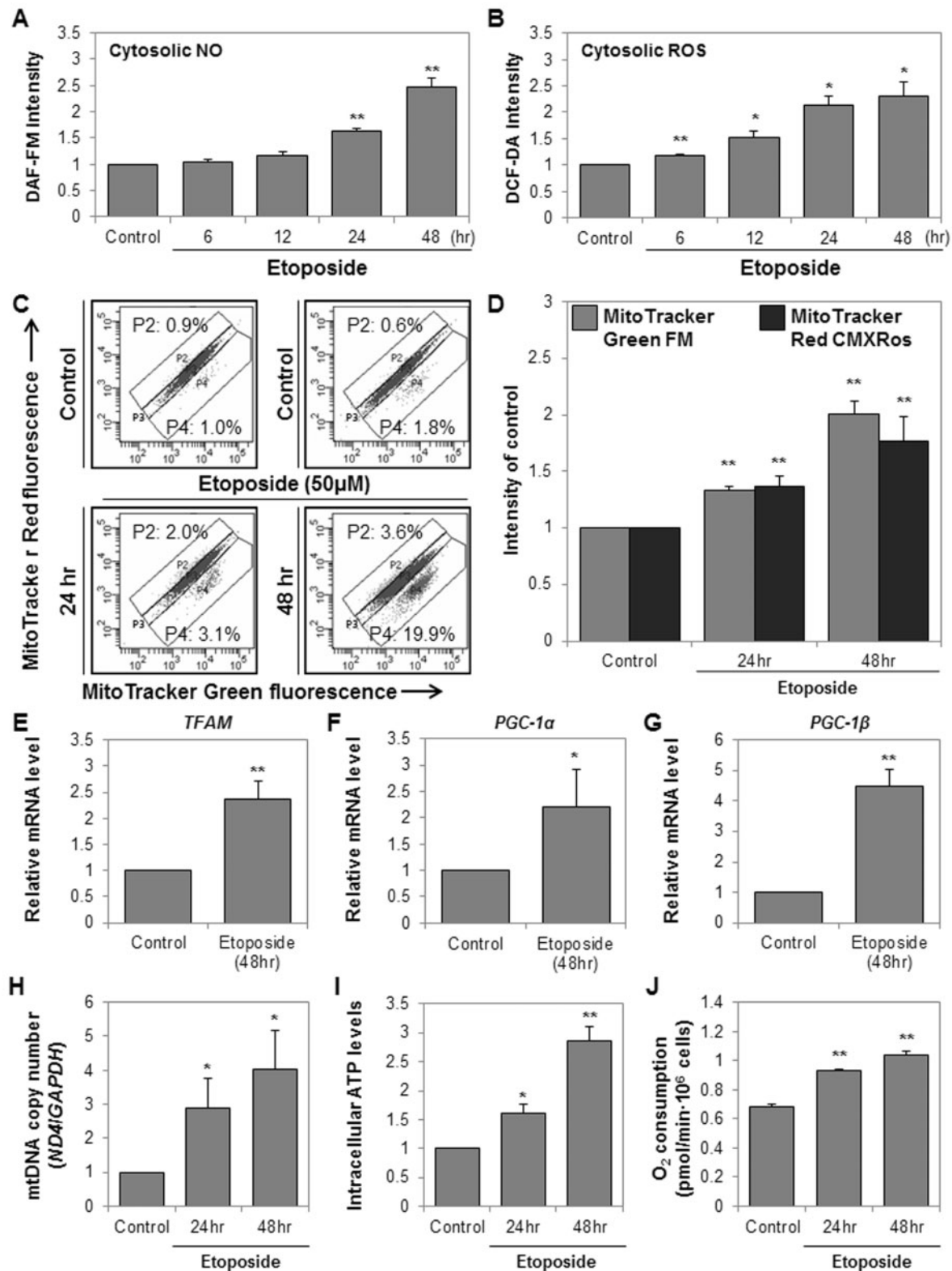


FIG. 2. Etoposide (ETO) induced generation of NO and reactive oxygen species (ROS) as well as mitochondrial biogenesis. A and B, DAF-FM and DCF-DA fluorescence intensity was examined to measure the generation of cytosolic NO and ROS, respectively, after the cells were incubated with ETO for different periods. C and D, The cells incubated with ETO for 24 and 48 h were double-stained with MitoTracker Red CMXRos and Green FM to analyze mitochondrial mass and respiration, respectively, using FACS analysis. The histogram represents mean intensity of MitoTracker Red CMXRos and Green FM fluorescence from 4 independent experiments. E–G, The mRNA expression levels of transcription factor genes (TFAM, PGC-1 α , and PGC-1 β) that are related to mitochondrial biogenesis were measured using real-time PCR. H, Genomic DNA obtained from ETO-treated HK-2 cells at 24 and 48 h was analyzed for mtDNA copy number using ND4 and GAPDH primers by means of real-time PCR. ND4 copy numbers were normalized to GAPDH and were analyzed relative to the copy numbers of the controls. I, After ETO treatment for 24 and 48 h, the cytosolic ATP levels were measured using the CellTiter-Glo Luminescent Cell Viability Assay. J, The oxygen consumption rate was measured after treatment with ETO for 24 and 48 h.

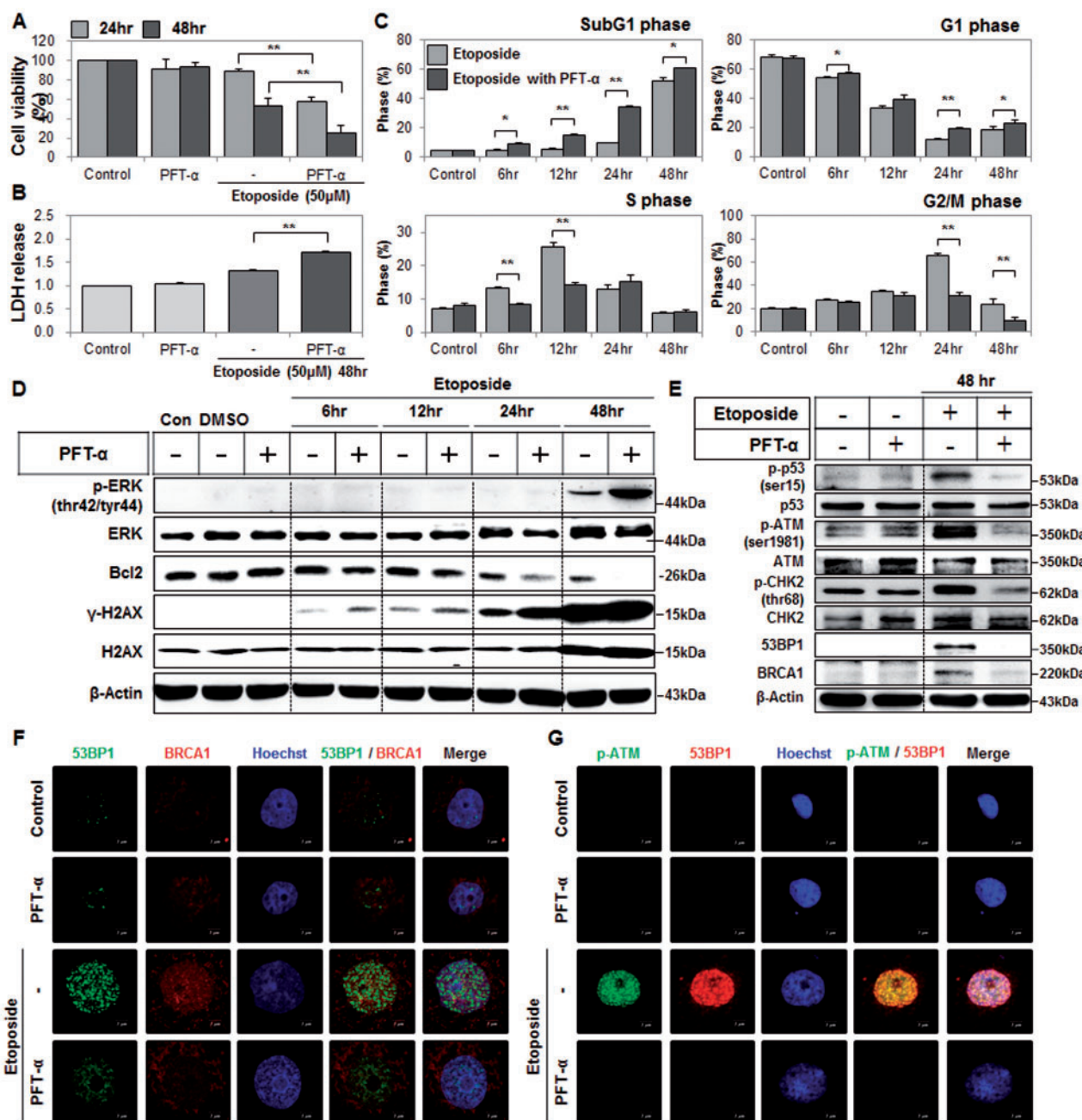


FIG. 3. Inhibition of p53 reduced cell viability and expression of DNA damage response (DDR) proteins and abrogated the cell cycle arrest. Cells were treated with etoposide (ETO) and/or PFT- α (p53 inhibitor) for the indicated periods. β -Actin was used as a loading control for Western blotting. A, Cell viability was analyzed using the MTT assay. B, Cytotoxicity was analyzed using the LDH assay. C, DNA content and a cell cycle arrest were detected using PI staining for the indicated periods. Representative histograms and the percentage of each cell cycle phase are shown. D and E, Expression levels of p-ERK^{thr42/tyr44}, ERK, Bcl2, γ -H2AX^{ser139}, H2AX, p-p53^{ser15}, p53, PARP1, p-ATM^{ser1981}, ATM, p-CHK2^{thr68}, CHK2, 53BP1, and BRCA1 were analyzed using Western blotting. F and G, Representative images of confocal microscopy are shown.

Western blot analysis. Inhibition of p53 rapidly induced the expression of γ -H2AX and phosphorylation of extracellular-signal-regulated kinase (p-ERK), but reduced the B-cell lymphoma (Bcl2) expression level in a time-dependent manner (Fig. 3D). A pharmacological ERK inhibitor, PD95059, which was coadministered with ETO, significantly reduced the expression levels of p-ERK and apoptotic C-PARP1 (89kDa) at 48h (Supplementary Fig. 5B) as well as caspase 3/7 activity, compared to the ETO-only control (Supplementary Fig. 5C). Moreover, the inhibition of p53 reduced the expression levels of DNA damage

transducer and repair proteins including p-ATM, p-CHK2, 53BP1, and BRCA1 (Fig. 3E). Immunofluorescence analysis showed that inhibition of p53 decreased the signal intensity of p-ATM, 53BP1, and BRCA1 in the nucleus (Fig. 3F and G).

Inhibition of p53 Affected Mitochondrial Biogenesis, Oxidative Stress, and Caspase 3 Activation

Inhibition of p53 during ETO treatment dramatically induced cytosolic NO production and secretion of NO (Fig. 4A and B), whereas p53 inhibition led to a considerable decrease in cROS

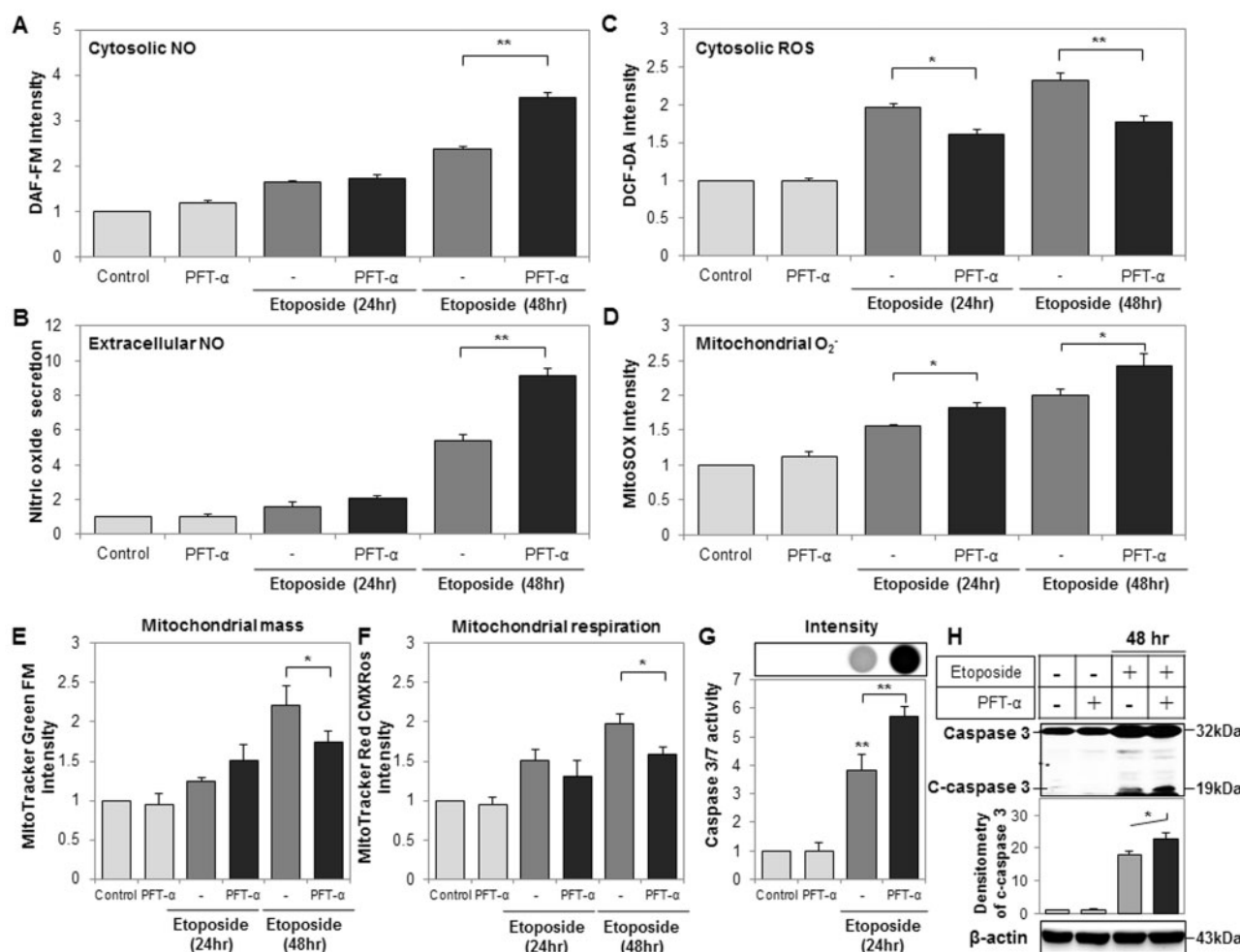


FIG. 4. Inhibition of p53 affected mitochondrial biogenesis, mitochondrial superoxide (O_2^-) accumulation, and caspase 3 activation. Cells were treated with etoposide (ETO) and/or PFT- α (p53 inhibitor) for the indicated periods. β -Actin was used as a loading control for Western blot analysis. A, Cytosolic NO generation was measured by means of DAF-FM fluorescence staining and FACS analysis. Representative histograms and fluorescence intensity are shown. B, Secretion of NO was measured using an NO detection kit, and the absorbance was analyzed on a microplate reader. Representative histograms and NO concentrations are shown. C, Cytosolic ROS generation was determined using DCF-DA fluorescence staining and FACS analysis. Representative histograms and the fluorescence intensity are shown. D, O_2^- accumulation in mitochondria was determined using MitoSOx fluorescence staining and FACS analysis. Representative histograms and O_2^- concentrations are shown. E and F, Mitochondrial mass and respiration were determined using MitoTracker Green FM and MitoTracker Red CMXRos staining, respectively, with FACS analysis. Representative histograms and the fluorescence intensity are shown. G, Activity of caspases 3 and 7 was determined by means of the Caspase-Glo 3/7 Assay using a luminescence reader; the image shows luminescence intensity. H, Cleaved-caspase 3 (C-caspase 3) expression levels were measured using Western blotting. The ratio of C-caspase 3 intensity is shown in the histogram.

production after ETO treatment (Fig. 4C). Inhibition of p53 significantly increased the O_2^- level in mitochondria after ETO treatment (Fig. 4D), but reduced mitochondrial respiration and mass (Fig. 4E and F). Contrary to our observation in cells treated with only ETO, we observed that the inhibition of p53 downregulated the Bcl2 expression level in a time-dependent manner. Bcl2 is an integral outer membrane mitochondrial protein that prevents mitochondrial cytochrome c release into the cytosol; thus, Bcl2 prevents caspase-mediated apoptosis (Yang et al., 1997). Guided by the literature, we examined the activity of caspases 3 and 7 and observed an increase 24 h after p53 inhibition and the start of ETO treatment (Fig. 4G). At 48 h, p53 inhibition resulted in an increase in protein expression levels of cleaved-caspase 3 (C-caspase 3) compared to the cells treated only with ETO (Fig. 4H).

Inhibition of p53 Disrupted Cell Adhesion and Induced Apoptosis

Using phase contrast microscopy, we found that ETO induced noticeable morphological changes, such as cellular and nuclear

swelling, whereas p53 inhibition caused cell shrinkage (Fig. 5A). Morphological features like cell swelling and a loss of plasma membrane integrity are associated with necrosis, whereas cell shrinkage and the development of apoptotic bodies are associated with apoptosis (Elmore, 2007). Thus, we concluded that ETO induces necrotic cell death, and inhibition of p53 triggers apoptotic cell death.

We assessed cell size regulation at different time points during ETO treatment and p53 inhibition using forward-scattered light analysis. Cells cotreated with ETO and PFT- α had an increase in cell size after 6 to 24 h; at 48 h, there was delayed cell swelling associated with a smaller cell size than that observed in cells treated with only ETO (Fig. 5B). Moreover, we analyzed the cell swelling and cell adhesion efficiency in ETO- plus PFT- α -treated cells using the xCELLigence system. The xCELLigence system utilizes a gold microelectrode device that allows for real-time impedance-based monitoring of cells, providing measurements of many cellular characteristics, including

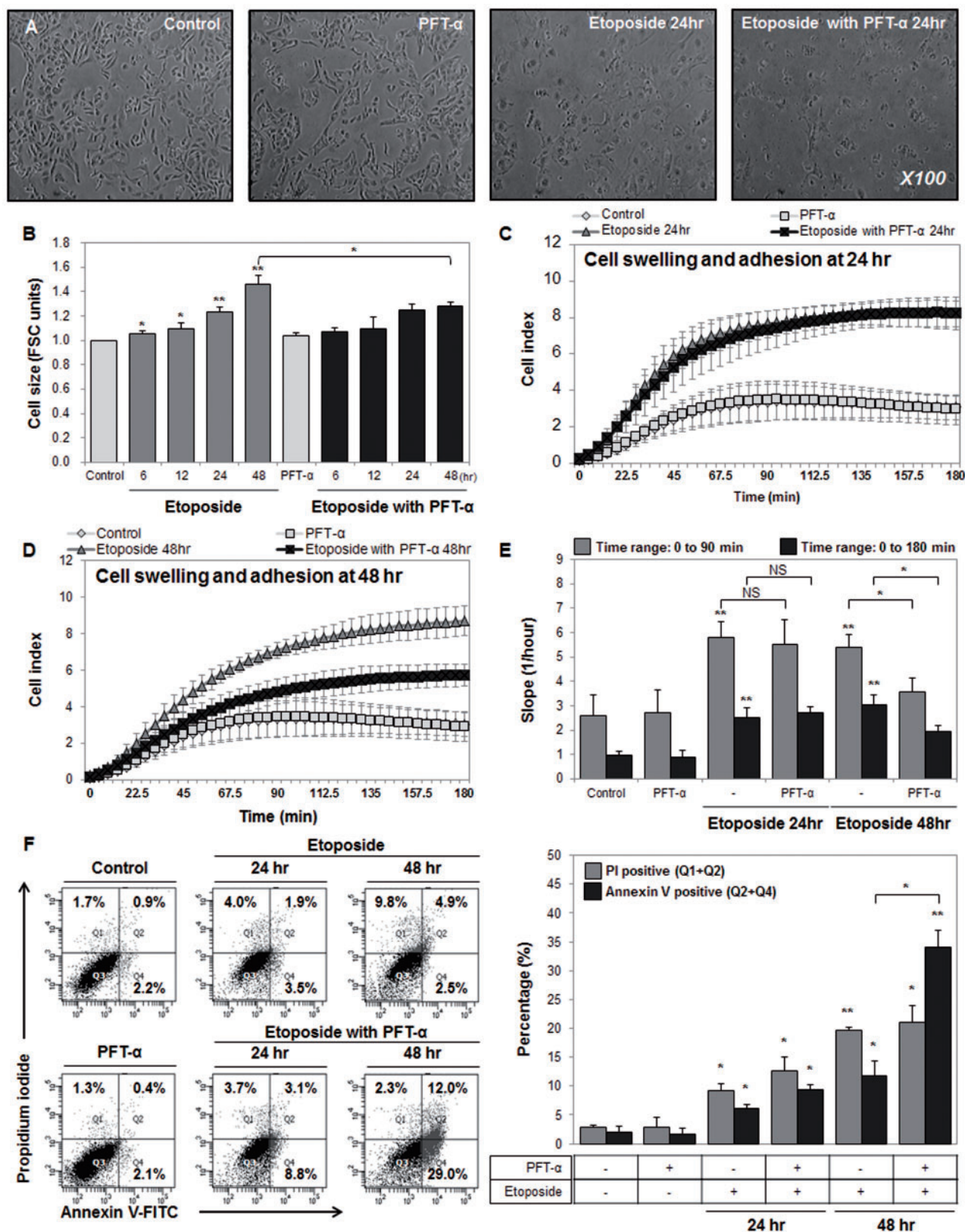


FIG. 5. Inhibition of p53 caused a loss of cell adhesion as well as apoptosis. HK-2 cells were treated with etoposide (ETO) and/or cotreated with PFT- α (p53 inhibitor) for the indicated periods. A, Morphological changes observed under a phase contrast microscope (original magnification was $\times 100$). B, The cell size was measured by means of FACS using forward-scattered light (FSC) analysis. C-E, End-point cell swelling and cell adhesion were analyzed using the xCelligence system at 10-s intervals over a period of 3 h, as shown in the line graphs. Slope (1/h) analysis was performed using the RTCA software and is presented in the histogram. An increasing slope indicates cell swelling and cell adhesion at 0 to 90 min and at 0-180 min. NS: not significant. F, Necrotic and apoptotic cell death were studied using FACS analysis after Annexin V/PI double fluorescent dye staining. Histograms represent the mean percentage of Annexin V-positive and PI-positive cells.

viability and cytotoxicity (Urcan *et al.*, 2010), and we modified the method to evaluate the adhesion efficiency. The treated cells were harvested and seeded in the device, which measures electrical impedance (cell index, which is proportional to cell adhesion) at 10-s intervals over a period of 3 h. The untreated control (HK-2 cells) and the PFT- α -treated group showed a cell index of 3.0 and 2.9 respectively, which reached saturation at 90 min. ETO treatment increased the cell index (after 24 h: 8.2; after 48 h: 8.7) and saturation time (at 24 h: 90 min; at 48 h: 117 min) compared to untreated control cells. On the other hand, inhibition of p53 reduced cell adhesion efficiency after 24 h, increasing the cell index (after 24 h 8.2; after 48 h 5.7) and saturation time (at 24 h: 112.5 min; at 48 h: 130.5 min; Fig. 5C and D). Similarly, slope analysis indicated that ETO induced cell swelling at 24 and at 48 h in early (0–90 min) and late (0–180 min) intervals. Inhibition of p53, however, had no significant effect at 24 h, and reduced cell adhesion in early (33.9%) and late (35.7%) intervals at 48 h of ETO treatment (Fig. 5E). Next, an Annexin V/propidium iodide (PI) double-staining method was used to analyze cell death processes by detecting apoptosis (Annexin V-positive cells) and necrosis (PI-positive cells). ETO-treated cells showed an increase in Annexin V- and PI-positive cells compared to the control in a time-dependent manner. In contrast, inhibition of p53 induced apoptotic cell death: a 2.3-fold increase in the number of Annexin V-positive cells after 48 h of incubation with ETO (Fig. 5F).

Inhibition of p53 Induced a Morphological Transition From Necrosis to Apoptosis

For the first time, morphological changes were directly visualized along with changes in plasma membrane topography (at a resolution of 1–45 μ m) related to necrotic and apoptotic cell death using CNT/AFM probes in ETO- and/or PFT- α -treated cells at 24, 36, and 48 h (Supplementary Fig. 6). The use of CNT/AFM probes is of particular interest for high-resolution imaging of biological materials such as DNA and proteins, due to the small diameter of the tube, strong mechanical properties, reversible elastic buckling, and chemical stability (Lee *et al.*, 2008; Wilson and Macpherson, 2009). AFM images revealed that ETO treatment created ruptures in the plasma membrane and caused cell swelling, which increased as time passed (Fig. 6A and Supplementary Video 1). After 48 h of ETO treatment, the height and width of the ruptures were 124.0 and 1,295.9 nm, respectively (Fig. 6C). Compared to cells treated with ETO only, the inhibition of p53 did not cause significant morphological changes after 24 h of ETO at a resolution of 45- μ m, although we did observe the formation of plasma membrane bubbles at a resolution of 5- μ m, which is representative of the early apoptotic stage (Fig. 6A). After 36 h, inhibition of p53 triggered significant cell shrinkage and the appearance of filopodia, which were observed at a resolution of 45- μ m. Analysis of plasma membrane topography revealed signs of necrosis-induced plasma membrane rupture with reduced height and width at a resolution of 5- μ m (Fig. 6A). Subsequently, the inhibition of p53 reliably triggered cell shrinkage, formation of filopodia, and the appearance of apoptotic bodies at 48 h (Fig. 6A and Supplementary Video 2). In particular, we detected apoptotic bodies of different size and volume (Fig. 6D), separated by collapsing boundaries (Fig. 6B).

A p53 Knockdown Reduced the cROS Generation and Induced Caspase 3 and Apoptosis

Experiments with a pharmacological inhibitor of p53 (PFT- α) showed that p53 regulated several processes, including caspase

3 activation and cROS generation. Both were detected during the initiation of apoptosis. To confirm, we knocked down (KD) p53 in HK-2 cells via transfection with p53 siRNA, and observed that p53 controlled cell viability, cROS generation, activation of caspases 3 and 7, and Annexin V intensity (Fig. 7). Results from the Western blot analysis revealed that the expression of p53 was suppressed successfully after transfection with 200 nM of the p53 siRNA; hence, the same concentration was used for subsequent experiments (Fig. 7A). P53KD cells had lower viability (reduction by 23.9%) and cROS generation (reduction by 15.3%) than the control, which was transfected with scrambled-siRNA (SC-siRNA; Fig. 7B and C). PARP1, C-PARP1 (89 kDa), and C-caspase 3 were significantly upregulated in the p53KD cells (Fig. 7D). Similarly, we found that p53 downregulation increased caspase 3/7 activity (by 38.1%) and Annexin V intensity (by 33.1%) to a higher level than did the control, SC-siRNA (Fig. 7E and F).

DISCUSSION

Cell death is commonly classified as being either apoptosis and necrosis using the morphological and biochemical characteristics of cell death (Elmore, 2007). Generally, morphological changes have been measured in gold- and platinum-coated samples and detected using a scanning electron microscope. This approach has 2 disadvantages: (1) indirect evidence and hectic preparation of samples, (2) difficulty describing the plasma membrane's topographic features. Here, we directly identified the effects of p53 inhibition and ETO on the regulation of necrotic and apoptotic morphological changes using CNT/AFM probes. Our results demonstrated that ETO could induce necrotic cell morphology, including cellular and nuclear swelling. Upon further examination of the topographical images of the plasma membrane, we saw that the height and width of plasma membrane ruptures gradually increased, and ultimately resulted in a cave-in. Inhibition of p53 did not affect cell swelling, but produced many bubbles in the plasma membrane after 24 h of ETO treatment, and did initiate cell shrinkage, filopodia, and signs of rupture at 36 h. After 48 h of ETO treatment preceded by p53 inhibition, the cells were clearly shrunken and had membrane bubbles compared to the cells treated with ETO alone. Our topographical imaging revealed that filopodia and apoptotic bodies surrounded the cell, forming 2 distinct structures with overlapping boundaries. Similarly, cell adhesion efficiency did not change significantly at 24 h, but decreased sharply at 48 h in cells treated with both ETO and a p53 inhibitor. Therefore, we can conclude that the ETO-induced damage led to necrosis during the initial stages but then switched to apoptosis at later stages. Expression of p53 suppressed ETO-induced apoptotic processes, thereby leading to necrosis and to changes in cell morphology. Furthermore, we believe that the CNT/AFM probe technique can effectively detect morphological changes associated with the early and late stages of necrosis and apoptosis, and that it can be used to easily and accurately measure cytotoxicity, cell differentiation, and organelle size in *in vitro* models.

Numerous studies reported that ETO enhanced apoptotic cell death in p53-deficient human non-small lung cancer and colon cancer cells (Chiu *et al.*, 2005; Mahyar-Roemer and Roemer, 2001). Moreover, p53-deficient MEF cells were sensitive to the ETO-induced apoptotic cell death when compared with wild-type of MEF cells (Shibue *et al.*, 2003). However, the mechanism by which p53 mediated the antiapoptotic processes and lead to necrosis are not fully understood. Our report shows that

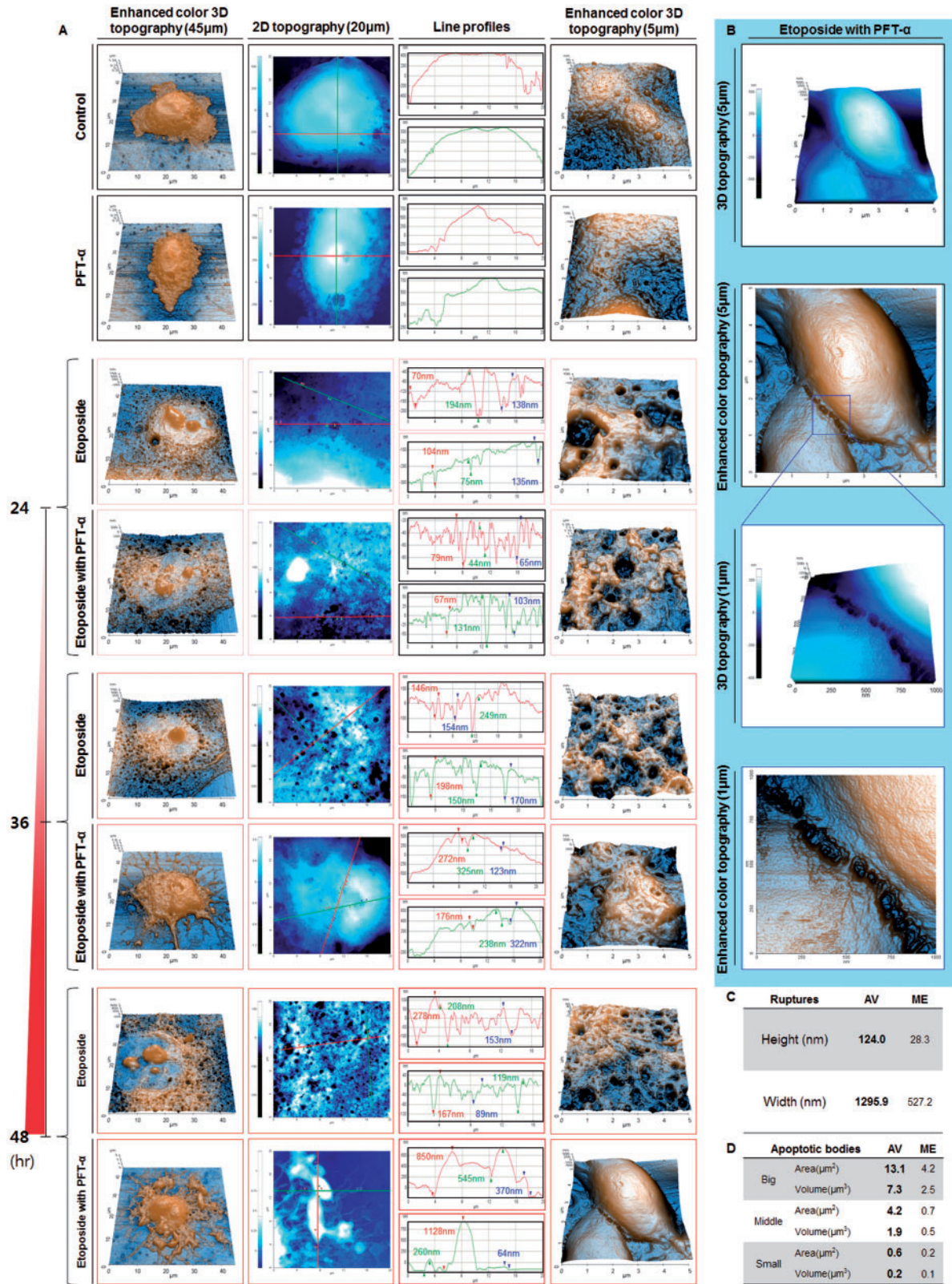


FIG. 6. Inhibition of p53 converted necrotic to apoptotic morphological changes. Morphological changes were examined using CNT/AFM probes after 24, 36, and 48 h of incubation with etoposide (ETO) and/or PFT-α (p53 inhibitor). See also Supplementary Fig. 6 and Videos 1 and 2. A, The image represents 3D topography (45 and 5 µm scale), 2D topography (20 µm scale), and line profiles (20 µm scale). Plasma membrane topography was analyzed (including red and green lines) using line profile analysis on the 20 µm scale. B, Apoptotic bodies on 3D topography and enhanced color (5 and 1 µm scale) in cells cotreated with ETO (48 h) and PFT-α. C and D, Height and width of plasma membrane ruptures as well as the area and volume of apoptotic bodies were analyzed using grain analysis in the XEI software (45 µm scale) for 48 h. The tables include average (AV) and mean error (ME) values.

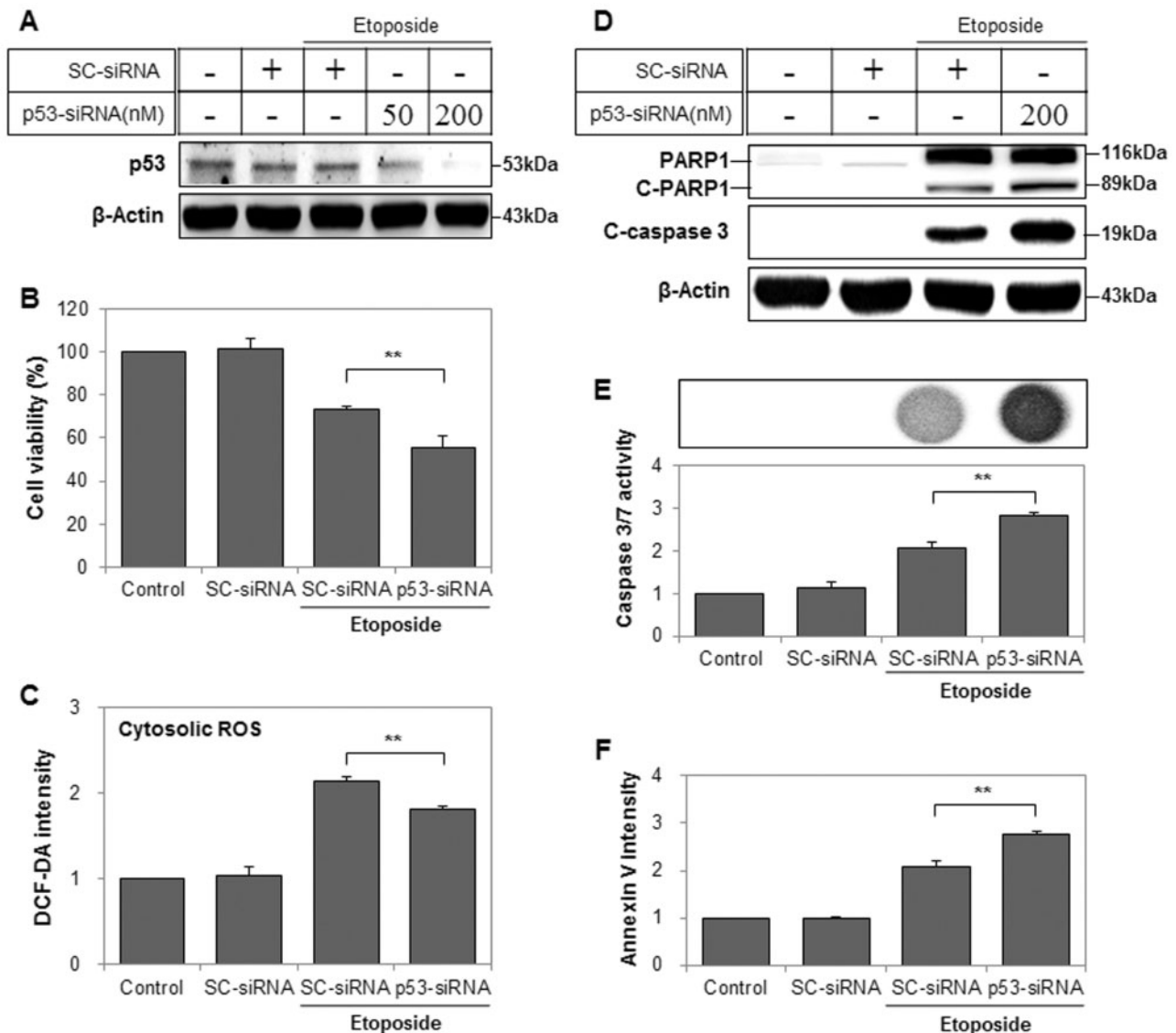


FIG. 7. A knockdown of p53 reduced the generation of cytosolic reactive oxygen species (cROS) and induced apoptosis. Scrambled control siRNA (SC-siRNA)- or p53 siRNA (p53-siRNA)-transfected cells were incubated with etoposide (ETO) for the indicated periods. β-Actin was used as a loading control for Western blot analysis. **A**, Expression levels of p53 were analyzed using Western blotting after the transfection with either 50 or 200 nM p53 siRNA. The subsequent experiments involved use of 200 nM p53-siRNA. **B**, Cell viability was analyzed using the MTT assay. **C**, Cytosolic ROS generation was determined by means of DCF-DA fluorescence staining and FACS analysis. **D**, PARP1, C-PARP1 (89 kDa), and cleaved-caspase 3 (C-caspase 3) expression levels were analyzed using Western blotting. **E**, Caspase 3/7 activity was determined using the Caspase-Glo 3/7 Assay and a luminescence reader. The top image shows luminescence intensity. **F**, Apoptotic cells were identified by means of Annexin V fluorescence staining and FACS analysis.

inhibition of p53 resulted in strong activation of apoptotic processes. Thus, we believe that p53 acts via 2 mechanisms: suppression of apoptotic processes, and promotion of ETO-induced necrosis (Fig. 8).

First, our results revealed that ETO treatment resulted in an increase in protein expression levels of DDR modulators, including sensor, transducer, effector, and DNA damage repair proteins. DNA damage repair classified into 2 main processes: homologous recombination (HR; BRCA1), and nonhomologous end joining (NHEJ; 53BP1), which compete for the repair of DNA breaks (Bunting et al., 2010; Roy et al., 2012). Double- and single-strand breaks are repaired via NHEJ in the G1 phase and via HR in the S and G2/M phase. Irreparable DNA damage leads to apoptosis (Branzei and Foiani, 2008). Similarly, ETO induced BRCA1 expression, and downregulated 53BP1 over the course of

the necrotic process during the S and G2/M phase arrest after 24 h of treatment. On the other hand, inhibition of p53 dramatically enhanced DNA damage and reduced the expression levels of the transducer and DNA damage repair proteins, as well as abrogated the ETO-induced S and G2/M phase arrest; these events converted cell death from necrotic to apoptotic. Previous studies showed that the DNA repair protein RAD51 homolog 1 (RAD51) and the DNA repair and recombination protein RAD54-like (RAD54) directly interact with p-p53^{ser15}, and suggested that p53 is a modulator of the HR-mediated repair process (Linke et al., 2003; Sengupta et al., 2003). IR-induced DNA damage increases the levels of p-p53^{ser15}, and that γ-H2AX and p-p53^{ser15} and p-p53^{ser15} and 53BP1 are co-localized in the nucleus, respectively (Al Rashid et al., 2005). They also demonstrated that a p53 point mutation at Ser¹⁵ decreases the

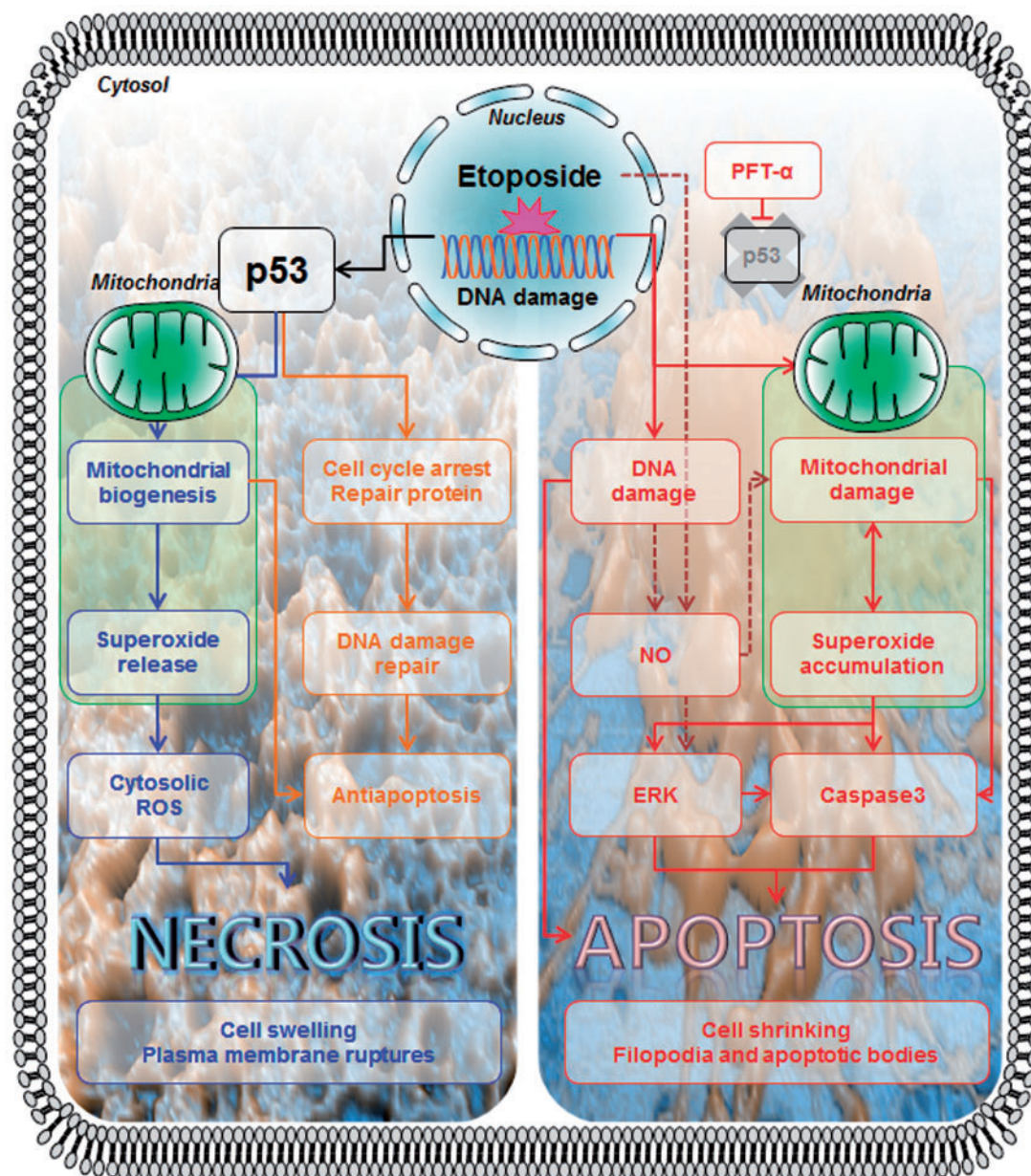


FIG. 8. An overview of p53-triggered antiapoptotic processes during etoposide-induced cell death.

expression of cyclin-dependent kinase inhibitor 1A (p21) and formation of γ -H2AX foci, and these events increase DNA fragmentation. Hence, our findings substantiate the crucial role p53 plays in contributing directly to DNA damage reorganization and DDR signaling pathway via induction of proteins involved in DNA damage repair and in cell cycle arrest, which protects against ETO-induced DNA damage and apoptosis. This process may result in resistance to chemotherapeutic drugs in cancer, and this resistance is primarily regulated by p-p53^{ser15}. In this context, we believe that ETO can potentially serve as an effective chemotherapeutic drug for patients with p53 mutations in different types of cancer; in fact, ETO may cause fewer adverse effects on healthy organs.

Second, our results show that ETO treatment stimulates mitochondrial biogenesis. In contrast, the inhibition of p53 reduces mitochondrial biogenesis by lowering mitochondrial

mass and respiration levels as a result of Bcl2 degradation, caspase 3 activation, and apoptosis. Our findings consistently show that ETO activates mitochondrial biogenesis through the ATM/AMP-activated protein kinase (AMPK) signaling pathway (Fu *et al.*, 2008). AMPK activator, 5-aminoimidazole-4-carboxamide-ribonucleoside (AICAR), induces PGC-1 expression and increases mitochondrial mass; these changes protect the staurosporine-induced activity of caspases 3 and 9 and apoptotic cell death (Dam *et al.*, 2013). Moreover, p53 knockout mice show a reduced mitochondrial yield, O₂ consumption rate, and PGC-1 expression level, as well as induced ROS generation in skeletal muscle (Saleem *et al.*, 2009). As shown in Fig. 4, the inhibition of p53 decreased cROS production and increased O₂⁻ concentration in mitochondria during apoptosis. The O₂⁻ generated by respiratory chain complexes in the mitochondrial inner membrane is released into the cytosol as ROS (Zhang and Guterman,

2007). Damage to mtDNA resulted in the generation of mitochondrial O_2^- and mitochondrial permeability-triggered apoptosis (Ricci et al., 2008), whereas O_2^- induced apoptosis via activation of caspase 3 (Jameel et al., 2009). Manganese superoxide dismutase (MnSOD), an important antioxidant enzyme that eliminates O_2^- , is reported to be elevated in chemoresistant ovarian cancer cells. Thus, the inhibition of MnSOD increases the production of O_2^- by the ovarian cancer cells and enhances DOX- and paclitaxel-induced activation of caspase 3, 9 as well as apoptotic cell death via ERK (Yeung et al., 2008). Chemotherapy, H_2O_2 , NO donor, and peroxynitrite (known as ONOO $^-$) induced apoptosis through activation of ERK in various cell lines (Cagnol and Chambard, 2010). In our study, the inhibition of p53 in ETO-treated cells led to a drastic increase in the expression of p-ERK as necrosis was converted to apoptosis at 48 h. H_2O_2 -treated HK-2 cells time-dependently increased the expression level of p-ERK after H_2O_2 treatment (Supplementary Fig. 5A). A pharmacological ERK inhibitor when coadministered with ETO significantly reduced the expression levels of C-PARP1 (89 kDa) as well as caspase 3/7 activity compared with the ETO-only control (Supplementary Fig. 5B and C). Moreover, we have previously reported evidence that the inhibition of p-ERK reduces cytotoxicity in DOX-treated HK-2 cells (Park et al., 2012). It has been reported that DOX-induced generation of ONOO $^-$ in the cytosol and mitochondria from NO reacting with O_2^- ultimately causes cell death (Mukhopadhyay et al., 2009). ONOO $^-$ triggers mitochondrial damage such as depletion of the mitochondrial respiratory chain and energy failure, eventually leading to apoptosis (Stewart and Heales, 2003). In particular, sodium nitroprusside (an NO donor) was found to induce the phosphorylation of ERK, but the inhibition of ERK reduced NO donor-induced apoptosis (Kawasaki et al., 2007). Our results demonstrated that NO production levels strongly enhanced mitochondrial damage and apoptosis in p53-deficient cells. Taken together, we present evidence that p53 directly or indirectly contributes to mitochondrial biogenesis, resulting in the release of mitochondrial O_2^- and an increase in cROS levels; these changes ultimately lead to the suppression of ETO-induced apoptosis. In addition, O_2^- accumulation in mitochondria and NO overproduction increase the levels of p-ERK, and thus enhance apoptosis, which is suppressed by p53 during ETO treatment.

In conclusion, our study showed that p53 protects against apoptosis and leads to etoposide-induced necrosis. In addition, high-resolution AFM images revealed that the ETO promotes necrosis but then switches to apoptosis by inhibition of p53 in HK-2 cells. Our results also showed that p53 directly or indirectly contributes to mitochondrial biogenesis and ROS generation. This work is expected to lead to the development of more effective and individualized treatment for chemotherapy-resistant tumors.

SUPPLEMENTARY DATA

Supplementary data are available online at <http://toxsci.oxfordjournals.org/>.

ACKNOWLEDGMENT

All the authors declared no competing interests.

FUNDING

Mid-Career Researcher Program through the National Research Foundation of Korea (2012R1A2A2A02016803),

Korea Health Technology R&D Project through the Korea Health Industry Development Institute (HI14C1992), and Priority Research Centers Program (NRF 2012-0006687).

REFERENCES

- Al Rashid, S. T., Delleire, G., Cuddihy, A., Jalali, F., Vaid, M., Coackley, C., Folkard, M., Xu, Y., Chen, B. P., Chen, D. J., et al. (2005). Evidence for the direct binding of phosphorylated p53 to sites of DNA breaks in vivo. *Cancer Res.* **65**, 10810–10821.
- Alexieva-Botcheva, K., and Anderson, C. W. (2012). p53. In *Encyclopedia of Signaling Molecules* (S. Choi, Ed.), Vol. 3, pp. 1332–1345. Springer, New York, NY.
- Bogacka, I., Xie, H., Bray, G. A., and Smith, S. R. (2005). Pioglitazone induces mitochondrial biogenesis in human subcutaneous adipose tissue in vivo. *Diabetes* **54**, 1392–1399.
- Bolte, S., and Cordelieres, F. P. (2006). A guided tour into subcellular colocalization analysis in light microscopy. *J. Microsc.* **224**, 213–232.
- Branzei, D., and Foiani, M. (2008). Regulation of DNA repair throughout the cell cycle. *Nat. Rev. Mol. Cell Biol.* **9**, 297–308.
- Bunting, S. F., Callen, E., Wong, N., Chen, H. T., Polato, F., Gunn, A., Bothmer, A., Feldhahn, N., Fernandez-Capetillo, O., Cao, L., et al. (2010). 53BP1 inhibits homologous recombination in Brca1-deficient cells by blocking resection of DNA breaks. *Cell* **141**, 243–254.
- Cagnol, S., and Chambard, J. C. (2010). ERK and cell death: mechanisms of ERK-induced cell death—apoptosis, autophagy and senescence. *FEBS J.* **277**, 2–21.
- Chiu, C. C., Lin, C. H., and Fang, K. (2005). Etoposide (VP-16) sensitizes p53-deficient human non-small cell lung cancer cells to caspase-7-mediated apoptosis. *Apoptosis Int. J. Program. Cell Death* **10**, 643–650.
- Dam, A. D., Mitchell, A. S., and Quadrilatero, J. (2013). Induction of mitochondrial biogenesis protects against caspase-dependent and caspase-independent apoptosis in L6 myoblasts. *Biochim. Biophys. Acta* **1833**, 3426–3435.
- Dasika, G. K., Lin, S. C., Zhao, S., Sung, P., Tomkinson, A., and Lee, E. Y. (1999). DNA damage-induced cell cycle checkpoints and DNA strand break repair in development and tumorigenesis. *Oncogene* **18**, 7883–7899.
- Elmore, S. (2007). Apoptosis: a review of programmed cell death. *Toxicol. Pathol.* **35**, 495–516.
- Fu, X., Wan, S., Lyu, Y. L., Liu, L. F., and Qi, H. (2008). Etoposide induces ATM-dependent mitochondrial biogenesis through AMPK activation. *PLoS One* **3**, e(2009).
- Gobeil, S., Boucher, C. C., Nadeau, D., and Poirier, G. G. (2001). Characterization of the necrotic cleavage of poly(ADP-ribose) polymerase (PARP-1): implication of lysosomal proteases. *Cell Death Differ.* **8**, 588–594.
- Haupt, S., Berger, M., Goldberg, Z., and Haupt, Y. (2003). Apoptosis—the p53 network. *J. Cell Sci.* **116**, 4077–4085.
- Hock, M. B., and Kralli, A. (2009). Transcriptional control of mitochondrial biogenesis and function. *Annu. Rev. Physiol.* **71**, 177–203.
- Jameel, N. M., Thirunavukkarasu, C., Wu, T., Watkins, S. C., Friedman, S. L., and Gandhi, C. R. (2009). p38-MAPK- and caspase-3-mediated superoxide-induced apoptosis of rat hepatic stellate cells: reversal by retinoic acid. *J. Cell. Physiol.* **218**, 157–166.

- Janicke, R. U., Sohn, D., and Schulze-Osthoff, K. (2008). The dark side of a tumor suppressor: anti-apoptotic p53. *Cell Death Differ.* **15**, 959–976.
- Kawasaki, T., Kitao, T., Nakagawa, K., Fujisaki, H., Takegawa, Y., Koda, K., Ago, Y., Baba, A., and Matsuda, T. (2007). Nitric oxide-induced apoptosis in cultured rat astrocytes: protection by edaravone, a radical scavenger. *Glia* **55**, 1325–1333.
- Kim, E. Y., Shin, H. Y., Kim, J. Y., Kim, D. G., Choi, Y. M., Kwon, H. K., Rhee, D. K., Kim, Y. S., and Choi, S. (2010). ATF3 plays a key role in Kdo2-lipid A-induced TLR4-dependent gene expression via NF-kappaB activation. *PLoS One* **5**, e14181.
- Kluza, J., Marchetti, P., Gallego, M. A., Lancel, S., Fournier, C., Loyens, A., Beauvillain, J. C., and Bailly, C. (2004). Mitochondrial proliferation during apoptosis induced by anticancer agents: effects of doxorubicin and mitoxantrone on cancer and cardiac cells. *Oncogene* **23**, 7018–7030.
- Lee, J. H., Kang, W. S., Choi, B. S., Choi, S. W., and Kim, J. H. (2008). Fabrication of carbon nanotube AFM probes using the Langmuir-Blodgett technique. *Ultramicroscopy* **108**, 1163–1167.
- Linke, S. P., Sengupta, S., Khabie, N., Jeffries, B. A., Buchhop, S., Miska, S., Henning, W., Pedoux, R., Wang, X. W., Hofseth, L. J., et al. (2003). p53 interacts with hRAD51 and hRAD54, and directly modulates homologous recombination. *Cancer Res.* **63**, 2596–2605.
- Mahyar-Roemer, M., and Roemer, K. (2001). p21 Waf1/Cip1 can protect human colon carcinoma cells against p53-dependent and p53-independent apoptosis induced by natural chemopreventive and therapeutic agents. *Oncogene* **20**, 3387–3398.
- McBride, H. M., Neuspiel, M., and Wasiak, S. (2006). Mitochondria: more than just a powerhouse. *Curr. Biol.* **16**, R551–R560.
- Meirhaeghe, A., Crowley, V., Lenaghan, C., Lelliott, C., Green, K., Stewart, A., Hart, K., Schinner, S., Sethi, J. K., Yeo, G., et al. (2003). Characterization of the human, mouse and rat PGC1 beta (peroxisome-proliferator-activated receptor-gamma co-activator 1 beta) gene in vitro and in vivo. *Biochem. J.* **373**, 155–165.
- Mukhopadhyay, P., Rajesh, M., Batkai, S., Kashiwaya, Y., Hasko, G., Liaudet, L., Szabo, C., and Pacher, P. (2009). Role of superoxide, nitric oxide, and peroxynitrite in doxorubicin-induced cell death in vivo and in vitro. *Am. J. Physiol. Heart Circ. Physiol.* **296**, H1466–H1483.
- Muller, P. A., and Vousden, K. H. (2013). p53 mutations in cancer. *Nat. Cell Biol.* **15**, 2–8.
- Nitiss, J. L. (2009). Targeting DNA topoisomerase II in cancer chemotherapy. *Nat. Rev. Cancer* **9**, 338–350.
- Park, E. J., Kwon, H. K., Choi, Y. M., Shin, H. J., and Choi, S. (2012). Doxorubicin induces cytotoxicity through upregulation of pERK-dependent ATF3. *PLoS One* **7**, e44990.
- Pieczenik, S. R., and Neustadt, J. (2007). Mitochondrial dysfunction and molecular pathways of disease. *Exp. Mol. Pathol.* **83**, 84–92.
- Polo, S. E., and Jackson, S. P. (2011). Dynamics of DNA damage response proteins at DNA breaks: a focus on protein modifications. *Genes Dev.* **25**, 409–433.
- Poyton, R. O., Ball, K. A., and Castello, P. R. (2009). Mitochondrial generation of free radicals and hypoxic signaling. *Trends Endocrinol. Metab.* **20**, 332–340.
- Ray, P. D., Huang, B. W., and Tsuiji, Y. (2012). Reactive oxygen species (ROS) homeostasis and redox regulation in cellular signaling. *Cell. Signal.* **24**, 981–990.
- Ricci, C., Pastukh, V., Leonard, J., Turrens, J., Wilson, G., Schaffer, D., and Schaffer, S. W. (2008). Mitochondrial DNA damage triggers mitochondrial-superoxide generation and apoptosis. *Am. J. Physiol. Cell Physiol.* **294**, C413–C422.
- Rogakou, E. P., Nieves-Neira, W., Boon, C., Pommier, Y., and Bonner, W. M. (2000). Initiation of DNA fragmentation during apoptosis induces phosphorylation of H2AX histone at serine 139. *J. Biol. Chem.* **275**, 9390–9395.
- Ross, W., Rowe, T., Glisson, B., Yalowich, J., and Liu, L. (1984). Role of topoisomerase II in mediating epipodophyllotoxin-induced DNA cleavage. *Cancer Res.* **44**, 5857–5860.
- Roy, R., Chun, J., and Powell, S. N. (2012). BRCA1 and BRCA2: different roles in a common pathway of genome protection. *Nat. Rev. Cancer* **12**, 68–78.
- Ryter, S. W., Kim, H. P., Hoetzel, A., Park, J. W., Nakahira, K., Wang, X., and Choi, A. M. (2007). Mechanisms of cell death in oxidative stress. *Antioxid. Redox Signal.* **9**, 49–89.
- Saleem, A., Adhihetty, P. J., and Hood, D. A. (2009). Role of p53 in mitochondrial biogenesis and apoptosis in skeletal muscle. *Physiol. Genomics* **37**, 58–66.
- Schneider, C. A., Rasband, W. S., and Eliceiri, K. W. (2012). NIH Image to ImageJ: 25 years of image analysis. *Nat. Methods* **9**, 671–675.
- Sengupta, S., Linke, S. P., Pedoux, R., Yang, Q., Farnsworth, J., Garfield, S. H., Valerie, K., Shay, J. W., Ellis, N. A., Wasylyk, B., et al. (2003). BLM helicase-dependent transport of p53 to sites of stalled DNA replication forks modulates homologous recombination. *EMBO J.* **22**, 1210–1222.
- Shibue, T., Takeda, K., Oda, E., Tanaka, H., Murasawa, H., Takaoka, A., Morishita, Y., Akira, S., Taniguchi, T., and Tanaka, N. (2003). Integral role of Noxa in p53-mediated apoptotic response. *Genes Dev.* **17**, 2233–2238.
- Soldani, C., Bottone, M. G., Pellicciari, C., and Scovassi, A. I. (2001). Two-color fluorescence detection of Poly (ADP-Ribose) Polymerase-1 (PARP-1) cleavage and DNA strand breaks in etoposide-induced apoptotic cells. *Eur. J. Histochem.* **45**, 389–392.
- Stewart, V. C., and Heales, S. J. (2003). Nitric oxide-induced mitochondrial dysfunction: implications for neurodegeneration. *Free Radic. Biol. Med.* **34**, 287–303.
- Urcan, E., Haertel, U., Styllou, M., Hickel, R., Scherthan, H., and Reichl, F. X. (2010). Real-time xCELLigence impedance analysis of the cytotoxicity of dental composite components on human gingival fibroblasts. *Dent. Mater.* **26**, 51–58.
- Vaseva, A. V., Marchenko, N. D., Ji, K., Tsirka, S. E., Holzmann, S., and Moll, U. M. (2012). p53 opens the mitochondrial permeability transition pore to trigger necrosis. *Cell* **149**, 1536–1548.
- Ventura-Clapier, R., Garnier, A., and Veksler, V. (2008). Transcriptional control of mitochondrial biogenesis: the central role of PGC-1alpha. *Cardiovasc. Res.* **79**, 208–217.
- Vousden, K. H., and Lane, D. P. (2007). p53 in health and disease. *Nat. Rev. Mol. Cell Biol.* **8**, 275–283.
- Weinberg, J. M. (2011). Mitochondrial biogenesis in kidney disease. *J. Am. Soc. Nephrol.* **22**, 431–436.
- West, A. P., Shadel, G. S., and Ghosh, S. (2011). Mitochondria in innate immune responses. *Nat. Rev. Immunol.* **11**, 389–402.
- Wilson, N. R., and Macpherson, J. V. (2009). Carbon nanotube tips for atomic force microscopy. *Nat. Nanotechnol.* **4**, 483–491.
- Yang, J., Liu, X., Bhalla, K., Kim, C. N., Ibrado, A. M., Cai, J., Peng, T. I., Jones, D. P., and Wang, X. (1997). Prevention of apoptosis

- by Bcl-2: release of cytochrome c from mitochondria blocked. *Science* **275**, 1129–1132.
- Yeung, B. H., Wong, K. Y., Lin, M. C., Wong, C. K., Mashima, T., Tsuruo, T., and Wong, A. S. (2008). Chemosensitisation by manganese superoxide dismutase inhibition is caspase-9 dependent and involves extracellular signal-regulated kinase 1/2. *Br. J. Cancer* **99**, 283–293.
- Zhang, D. X., and Gutterman, D. D. (2007). Mitochondrial reactive oxygen species-mediated signaling in endothelial cells. *Am. J. Physiol. Heart Circ. Physiol.* **292**, H2023–H2031.